Dimensionality-Decomposition Based Deep Learning Approach for Non-Equilibrium Electric Double Layer Modeling

Weijie Li(李伟杰)[1], Yajie Li(李亚捷)[2], Maxim Avdeev[3], and Siqi Shi(施思齐)[2,4*]

[1]*State Key Laboratory of Materials for Advanced Nuclear Energy & Qianweichang College, Shanghai University, Shanghai 200444, China*
[2]*State Key Laboratory of Materials for Advanced Nuclear Energy & School of Materials Science and Engineering, Shanghai University, Shanghai 200444, China*
[3]*School of Chemistry, The University of Sydney, Sydney, New South Wales 2006, Australia*
[4]*Materials Genome Institute, Shanghai University, Shanghai 200444, China*

(Received 17 August 2025; accepted manuscript online 24 October 2025)

The electric double layer (EDL), formed by charge adsorption at the electrolyte–electrode interface, constitutes the microenvironment governing electrochemical reactions. However, due to scale mismatch between the EDL thickness and electrode topography, solving the two-dimensional (2D) nonhomogeneous Poisson–Nernst–Planck (N-PNP) equations remains computationally intractable. This limitation hinders understanding of fundamental phenomena such as curvature-driven instabilities in 2D EDL. Here, we propose a dimensionality-decomposition strategy embedding a fully connected neural network (FCNN) to solve 2D N-PNP equations, in which the FCNN is trained on key electrochemical parameters by reducing the electrostatic boundary into multiple equivalent 1D representations. Through a representative case of $LiPF_6$ reduction on lithium metal half-cell, nucleus size is unexpectedly found to have an important influence on dendrite morphology and tip kinetics. This work paves the way for bridging nanoscale and macroscale simulations with expandability to 2D situations of other 1D EDL models.

DOI: 10.1088/0256-307X/42/12/120803 CSTR: 32039.14.0256-307X.42.12.120803

The electrical double layer is the pivotal microenvironment that governs electrochemical reaction kinetics and critically influences the dynamic behaviors of electronic, biological, and electrode reaction systems.[1–5] The nonequilibrium electrical double layer (NEDL) incorporates Faradaic current, so that ion flux driven by both diffusion and electromigration remains permanently out of equilibrium. By establishing steep ionic concentration gradients and significant interfacial potential drops, the NEDL critically reduces activation barriers for electron transfer reactions. In turn, NEDL is governed by multiple factors, including the surface electric potential, electrode characteristics (such as topography, electrochemical potential and surface energy), electrolyte composition, solvent structure, temperature, and electrolyte concentration.[6–8] Accurate and quantitative representation of NEDL is essential for more realistic modeling of electrochemical reactions. Detailed investigations have covered multiple aspects of one-dimensional (1D) NEDL systems, including transient processes, reaction cascades, and size effects of the electrode.[9–15] Meanwhile, understanding of the NEDL on more complex electrode characteristics has also witnessed substantial research advances.[16,17]

However, it is difficult for the existing models to accurately represent the NEDL on the dynamically evolving electrode surfaces of arbitrary morphology. This limitation is tied to the fact that Gauss's law couples the curvature of the electrode to charge density, a relation that cannot be captured by 1D models. Fundamentally, the significant disparity in the profile length of physical quantities along normal versus tangential directions, which is inherent to two-dimensional (2D) NEDL systems, renders numerical approaches computationally intractable. This limitation hinders quantitative modeling of 2D interface-governed phenomena including the effect of surface charge enrichment on reactions or lithium dendrite growth.

For modeling NEDL both at nanoscale along the normal direction and at macroscale in the tangential direction, we propose a strategy that reduces the macroscale tangential dimensionality of electrochemical data, enabling a fully connected neural network (FCNN) to solve 2D NEDL in 1D space. This is achieved by decomposing the 2D NEDL into a set of discrete 1D NEDLs. The decomposition is performed by introducing an equivalent electrostatic boundary length L which forms a bijective mapping with net charge density σ at the electrode surface. This decomposition resolves the computational challenges associated with scale disparities by solving 2D NEDL in 1D space. Critically, the original 2D NEDL can be reconstructed without loss under the bijective mapping between L in 1D NEDL and σ in 2D NEDL (we ignore the lateral diffusion in 2D NEDL, which is later proven to be permissible). Numerical

*Corresponding author. Email: sqshi@shu.edu.cn
© 2025 Chinese Physical Society and IOP Publishing Ltd. All rights, including for text and data mining, AI training, and similar technologies, are reserved.

solutions for 1D NEDL are obtained via Newton–Raphson iteration backward from the diffusion layer boundary x_0 [calculation methods are detailed in Note 1 of the Supplementary Materials (SM)].

The use of a FCNN allows for the efficient resolution of the extensive decomposition set derived from the 2D NEDL, greatly accelerating its overall simulation. The FCNN establishes the functional mapping across the solution space of the 1D nonhomogeneous Poisson-Nernst-Planck (N-PNP) system, transforming the input parameters including ion concentrations c_i^0 at x_0, transition state activity coefficient γ_t, surface potential Φ_0 and L into boundary potential Φ_1 at x_0. Reaction rate v is derivable from L and Φ_1 via Eq. (S9) of the SM. This mapping $\mathcal{F}' : (\Phi_0, \gamma_t, c_i^0, L) \mapsto v$ directly generates an exact 1D NEDL decomposition set corresponding to the original 2D NEDL solution (deep learning parameters are detailed in SM Note 2). By integrating phase field modeling to compute the 2D NEDL boundary conditions (γ_t, c_i^0, L), the trained FCNN then outputs Φ_1 and v on the electrode surfaces. Driven by nanoscale 2D NEDL dynamics, this strategy simulates kinetics of 2D microscale interfacial phenomena such as the influence of tip effects and 2D dendrite growth (it is the same for 3D phenomena).

To illustrate this strategy, the half-cell reduction of $LiPF_6$ on a lithium metal electrode with a Li/Li^+ equilibrium reference electrode is considered. Only monovalent anions (c_-) and lithium ions (c_{Li^+}) are considered, and the activity coefficients are set as one for simplicity. In the Gouy–Chapman–Stern theory, the source term of the Poisson equation obeys the Boltzmann distribution in the diffusion layer.[18,19] This distribution requires the balance between the diffusion flux $J_{diffu} = -D_i \nabla c_i$ and the electromigration flux $J_{elec} = \frac{z_i D_i F}{RT} c_i \nabla \Phi$ ($c_i = \{c_-, c_{Li^+}\}$), where F is the Faraday constant, R is the ideal gas constant and T is temperature. Yet, a steady state under equilibrium can only be achieved when the electrode reaction rate is zero. Therefore, the source term for the Poisson equation in the N-PNP equations is given as $-\frac{F}{\varepsilon_r \varepsilon_0} \sum_i z_i c_i$ in the diffusion layer and zero in the Stern layer. $\varepsilon_r \varepsilon_0$ is the dielectric constant, and z_i is the charge number. We ignore specifically adsorbed ions, so concepts such as the inner Helmholtz interface and the potential of zero charge are not discussed in this paper. The source term of the transport equation can be stated as Eq. (S39) in SM, considering the reduction of Li^+ in the half-cell. Thus, the equations of 2D N-PNP system are expressed as follows:

$$\nabla^2 \Phi = -\frac{F}{\varepsilon_r \varepsilon_0} \sum\nolimits_i z_i c_i, \tag{1}$$

$$\frac{\partial c_{Li^+}}{\partial t} = \nabla \cdot \left(\nabla c_{Li^+} + \frac{D_s F}{RT} c_{Li^+} \nabla \Phi \right) - \frac{k_0}{\gamma_t} c_{Li^+}^{stern} e^{\frac{-\alpha F (d^{stern} E - E^{\ominus})}{RT}}, \tag{2}$$

$$\frac{\partial c_-}{\partial t} = \nabla \cdot \left(D_s \nabla c_- + \frac{z_i D_s F}{RT} c_- \nabla \Phi \right), \tag{3}$$

where d^{stern} denotes the thickness of the Stern layer, E represents the electric field strength at the Stern layer, $d^{stern}E$ corresponds to the potential difference $\Delta\Phi$ in the Stern layer, and $c_{Li^+}^{stern}$ is the lithium ion concentration at the Stern layer boundary. To overcome the reaction energy barrier for lithium ion reduction, $d^{stern}E$ needs to fall below the equilibrium potential difference.[20] Consequently, the reduction rate is negligibly low until sufficient charge accumulates within the NEDL. Accordingly, we neglect the transient process before the 2D NEDL reaching a steady state. The above assumption results in $\frac{\partial c_-}{\partial t} = 0$ and $\frac{\partial c_{Li^+}}{\partial t} = 0$ within the 2D NEDL for each time step of the phase field simulation. However, it should be noted that ions are still transported in the electrolyte bulk region outside the 2D NEDL, where the Φ_1 serves as the electrostatic boundary condition.

Figures 1(a)–1(d) present the distribution of relative ion concentrations ($\frac{c_i}{c_0}$) and potential (Φ) in 1D NEDL. As derived from Eq. (3), c_- in the steady state 1D NEDL still follows the Boltzmann distribution [see Fig. 1(b)]. However, equation (2) reveals that $c_{Li^+}^{stern}$ is consumed through reduction, preventing the 1D NEDL system from attaining a Boltzmann distribution in the steady state. It requires lithium ion concentration lower than the equilibrium value [Fig. 1(b)], ensuring that the diffusion flux J_{diffu} remains smaller than the electromigration flux J_{elec} to sustain continuous Li^+ reduction. Simultaneously, this implies that the applied potential difference is not completely dissipated across the 1D NEDL, leaving a residual potential drop across the bulk electrolyte region (see Fig. S5 in the SM; we assume that the condition of electrical neutrality is satisfied outside the NEDL). This residual potential, later quantified by the virtual parameter L, sustains the ionic migration current required for steady state reduction. Meanwhile, the steady state condition dictates that the electromigration rate at x_0 equals v (calculation methods are detailed in SM Note 1).

The inherent nanometer length scale of 1D NEDL [see Fig. 1(d)] is several orders of magnitude smaller than electrode topography (microns to millimeters).[21–23] The 2D NEDL system can be projected pointwise to tailored 1D NEDL representations which encode local interfacial properties. The 2D parameters including electrostatic boundary conditions, $c_{Li^+}^0$, c_-^0, Φ_0, and γ_t require projection onto the 1D NEDL systems to compute local solutions across the 2D electrode surface. While $c_{Li^+}^0$, c_-^0, and γ_t undergo direct dimensionality collapse from 2D NEDL boundaries, morphology-sensitive features such as curvature κ_0 and heterogeneity of net charge $\sigma(r)$, demand physics-informed reduction kernels [Eq. (5)] for spatial information compression.

Considering the equipotential condition on the electrode surface,

$$\Phi(r, \rho)|_{\rho=0} = \Phi_0, \tag{4}$$

where ρ denotes the 1D Cartesian coordinate within the 1D NEDL and r represents the 1D natural coordinate along the tangential direction of the electrode surface in the 2D NEDL. The boundary potential of the counter electrode (Li/Li^+ equilibrium electrode) is set to zero. The final task is to define the electrostatic boundary condition

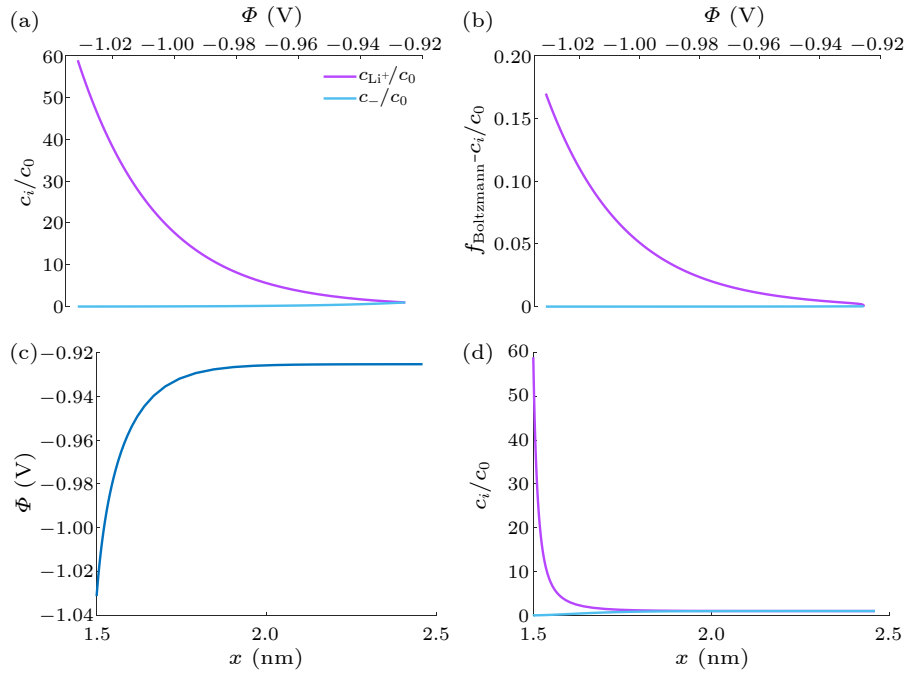

Fig. 1. Distributions of relative ion concentrations and electric potential under the following conditions: $\Phi_0 = -4.04\,\mathrm{V}$, c_-^0 and $c_{\mathrm{Li}+}^0 = 1\,\mathrm{mol/L}$, $d^{\mathrm{stern}} = 1.5\,\mathrm{nm}$, $L = 10\,\mu\mathrm{m}$, the bulk standard concentration is $c_0 = 1\,\mathrm{mol/L}$. (a) Distribution of $\frac{c_i}{c_0}(\Phi)$. (b) Deviation of distributions $\frac{c_i}{c_0}(\Phi)$ from the Boltzmann distribution $f_{\mathrm{Boltzmann}}(\Phi)$. (c) Distribution of $\Phi(x)$. (d) Distribution of $\frac{c_i}{c_0}(x)$.

for the 1D NEDL solution, which requires explicitly accounting for the effect of curvature-induced net charge heterogeneity. We implement this incorporation by fixing $\Phi(r,\rho_0)|_{\rho_0=L+x_0} = 0$, at the equivalent electrostatic boundary length $L = \rho_0 - x_0$. When $\sigma(r)$ is specified, L within the 1D NEDL has a unique solution:

$$L(r) = \frac{\varepsilon_{\mathrm{r}}\varepsilon_0\Phi_1}{\sigma(r)}, \tag{5a}$$

$$L(r) = -\frac{\Phi_1}{\nabla^2\Phi(r)}. \tag{5b}$$

$L(r)$ is defined by Eq. (5a) based on nanoscale electrostatic relations, yet by using microscale field quantities it is operationally calculated from Eq. (5b). Note that $L(r)$ in Eq. (5a) is an internal variable representing the plate separation of a virtual parallel-plate capacitor sustaining a potential difference of $\Delta\Phi = \Phi_1$, and it is determined through an iterative procedure described later. $\sigma(r)$ encodes 2D information about the electrode surface morphology and electrostatic boundary conditions. It is derived from the divergence of the electrode surface potential on a microscale under the electrostatic boundary conditions $\Phi(r,\rho)|_{\rho=x_0} = \Phi_1(r)$. It is also the net charge density of 2D NEDL at the point r. Equation (5a) intrinsically expresses the 1D Gauss's law, where the net charge density $\sigma(r)$ is derived from the 2D mesoscopic electrostatic field via $\sigma(r) = \varepsilon_{\mathrm{r}}\varepsilon_0\nabla^2\Phi(r)$. This constructs a dimensionality-reducing bridge from 2D continuous field to discrete 1D NEDL boundary parameters.

The resolved 2D information can be preserved during dimensionality decomposition by prescribing the $L(r)$ in 1D NEDL as stated in Eq. (5). This operator maintains the electric field equivalence $E(r,x_0)_{1\mathrm{D}} = E_{\partial\Omega_{2\mathrm{D}}}(r)$ while automatically ensuring compliance with Gauss's law during 2D reconstruction through the self-consistent charge density solution $\sigma(r) = -\varepsilon_{\mathrm{r}}\varepsilon_0\nabla^2\Phi(r)$. The $L(r)$ encodes the curvature effects $\kappa_0(r)$ via the the non-local relationship $\nabla^2\Phi(r) = f(\kappa_0, \nabla\kappa_0, \ldots) + g$ (boundary conditions). Although no universal analytical σ–κ_0 relation exists, our computational strategy resolves $\sigma(r)$ from $\nabla^2\Phi(r)$ [Eq. (5)] without explicit input of κ_0. This allows $L(r)$ to implicitly embed morphology through potential field divergence. Critically, due to the fact that $L(r)$ is not a physical length, it may exceed x_0 by several orders of magnitude depending on $\sigma(r)$.

A dimension reduction strategy for the 2D NEDL can be established from Eqs. (4) and (5). To characterize the solution space of the 1D NPNP, a uniform dataset is generated by randomized sampling within the physically admissible ranges of electrochemical parameters: v, $c_{\mathrm{Li}^+}^0$, γ_{t}, L, Φ_0, and Φ_1. The integration of domain knowledge rooted in transition state theory into our data preprocessing pipeline enables the construction of a homogeneous and linear solution space for universal mapping $\mathcal{F} : (\Phi_0, \gamma_{\mathrm{t}}, L, c_{\mathrm{Li}^+}^0) \mapsto \Phi_1$ (see SM Note 2).[24] Subsequently, an FCNN is trained using Φ_0, $c_{\mathrm{Li}^+}^0$, L, and γ_{t} as inputs with Φ_1 as output. The trained model computes overall distributions of v across the 2D NEDL for arbitrary spatial variations of inputs, in which v is derived from Φ_1 via Eq. (S9) of the SM (deep learning parameters are detailed in SM Note 2).

Notably, L is sampled in the solution space due to its strong impact on 1D NEDL. However, the mutual dependence between Φ_1 and L creates a computational deadlock: through Eq. (5), L is derived from Φ_1, while Φ_1 depends

on L via the FCNN mapping $\mathcal{F}$. To break this interdependency, we recast Eq. (5) as a physical constraint, enabling an iterative refinement loop

$$L(r)^k = \frac{\varepsilon_r\varepsilon_0\Phi_1(r)^k}{\sigma^{k-1}(r)\left\{1+n\times\tanh\left[\frac{1}{n}\left(\frac{\sigma^k(r)}{\sigma^{k-1}(r)}-1\right)\right]\right\}} \quad (6)$$

starting from

$$L(r)^0 = \frac{\varepsilon_r\varepsilon_0\Phi_0}{\sigma_0(r)}$$

and

$$\Phi_1(r)^k = \mathcal{F}(\Phi_0, \gamma_t, L(r)^{k-1}, c^0_{Li^+}).$$

Iteration continues until both $\max|1-\frac{L(r)^{k-1}}{L(r)^k}| < \varepsilon$ and $k > k_{min}$ with a proper relaxation factor n ensuring convergence (we set $\varepsilon = 0.005$ and $k_{min} = 50$, and investigate stability at different n in SM Note 2). The hyperbolic tangent function is also used to constrain the magnitude of iterative step to promote stability in the process of convergence.

In this iteration, the initial state is pure microscale 2D electrical field without considering 2D NEDL. This is captured by the initial guess $L(r)^0 = \frac{\varepsilon_r\varepsilon_0\Phi_0}{\sigma_0(r,\rho)|_{\rho=0}}$ and $\sigma_0(r) = -\varepsilon_r\varepsilon_0\nabla^2\Phi(r)$ with $\Phi(r,\rho)|_{\rho=x_0} = \Phi_0$. At each step k, tangential electric field coupling between 1D NEDLs are conceptually isolated by $\Phi_1(r)^k = \mathcal{F}(\Phi_0, \gamma_t, L(r)^{k-1}, c^0_{Li^+})$ and then reintroduced by $L(r)^k$ according to Eq. (6) under the more accurate $\Phi_1(r)^k$. Through iterations, these updates model the charge rearrangement dynamics arising from the inclusion of the 2D NEDL into the initially coupled electrostatic background.

The above discussion ignores the lateral diffusion; however, the non-uniform σ across the 2D electrode surface leads to a tangential gradient of anion and cation concentration in the 2D NEDL. These concentration gradients drive lateral ionic diffusion, generating a lateral electric field. The lateral electric field redistributes the charge in 2D NEDL and imparts additional potential energy to the anions and cations. A steady state is achieved when the additional potential energy is balanced by the chemical energy arising from the lateral ion concentration gradient.

Figure 2 illustrates the impact of lateral diffusion on the effective ion concentration: $c_e(r) = \frac{1}{x_0}\int_0^{x_0} c_{Li^+}(r,\rho) - c_-(r,\rho)\mathrm{d}\rho$ in the 1D NEDL under different ratios (N) of c_e and characteristic length ($4C$) of charge density variation. The distribution of $c_e(r)$ before lateral diffusion is set as $\{\frac{N-1}{2}[\tanh(r/C)+1]+1\}^{-1}$.

Figure 2 reveals subtle variations in ion concentration compared to the initial distribution (see SM Fig. S1). Consequently, the lateral diffusion of ion concentrations within 2D NEDL becomes negligible below the micrometer scale (see SM Note 3 for details).

In practical batteries, the dynamic nature of electrode reactions can cause the boundary conditions of the 2D NEDL to vary with the electrochemical processes. Prevailing phase field model [25–30] can simulate the evolution of coupled 2D fields in batteries. However, these approaches neglect the NEDL and erroneously equate the driving potential for electrode reactions to the externally applied potential difference rather than the true interfacial potential drop. [30] Therefore, we adjust the phase field model to calculate the boundary conditions of 2D NEDL(see SM Note 4 for details). The parameters taken from literatures [30,31] are shown in Table 1.

We now discuss the influence of Φ_0, $c^0_{Li^+}$, γ_t^{-1}, and σ on v, as well as the influence of 2D NEDL on the growth of 2D dendrites. Compared to Φ_0, L, and $c^0_{Li^+}$, γ_t^{-1} has a negligible effect on Φ_1 [32] in this case.

Figure 3(a) shows a linear correlation between the current density ($j = Fv$) and the Li^+ concentration ($c^0_{Li^+}$), which is consistent with experimental observations. [33] From Eq. (S9) of the SM and Fig. 3(b), it is seen that j exhibits gradual deviation from linear growth at elevated ion concentration, manifesting a saturation effect. Concentration-dependent suppression of Φ_1 becomes non-negligible at low $c^0_{Li^+}$ or sufficiently positive Φ_1 as shown in Fig. 3(b).

Table 1. Parameters employed to model 2D NEDL from a $LiPF_6$ electrolyte.

Parameter	Symbol	Value
Barrier height	W	$3.75\times10^5\,\mathrm{J/m^3}$
Gradient energy coefficient	κ	$5\times10^{-5}\,\mathrm{J/m}$
Standard rate constant	k_0	$8.3\times10^{-5}\,\mathrm{m/s}$
Diffusion coefficient in solution	D_s	$7.5\times10^{-10}\,\mathrm{m^2/s}$
Diffusion coefficient in electrode	D_e	$7.5\times10^{-13}\,\mathrm{m^2/s}$
Relative dielectric constant	ε_r	8
Thickness of the Stern layer	d^{stern}	1.5 nm

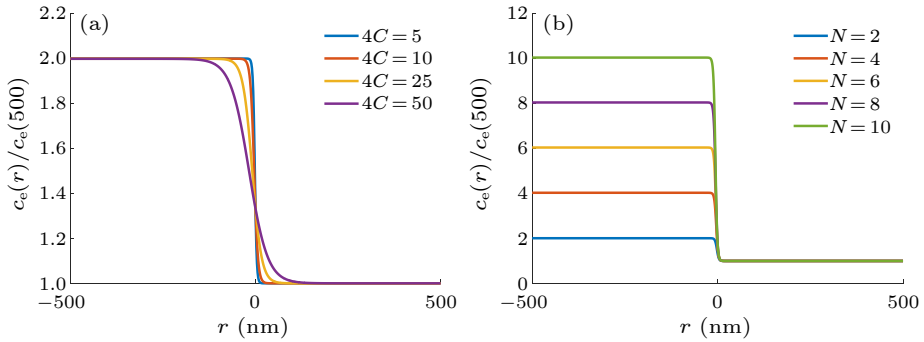

Fig. 2. Distributions of $c_e(r)$ after lateral diffusion with the fixed parameters are set to $N = 2$ and $4C = 20$. (a) Distributions of $c_e(r)$ for different characteristic lengths $4C$. (b) Distributions of $c_e(r)$ for different ratios N.

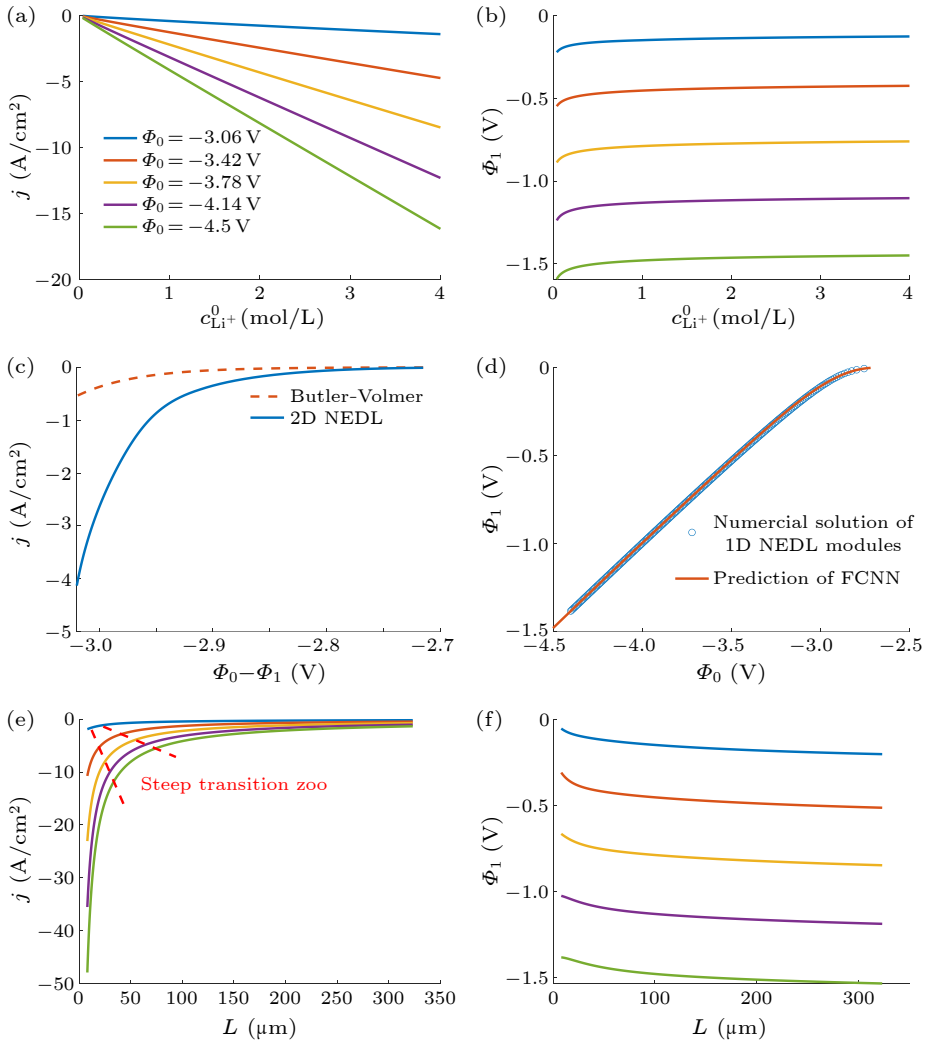

Fig. 3. The mapping of electrochemical factors with the fixed parameters are set to: $c^0_{\mathrm{Li}^+} = 1\,\mathrm{mol/L}$, $L = 100\,\mu\mathrm{m}$, and $\gamma_t^{-1} = 1$. (a) Variation of j with $c^0_{\mathrm{Li}^+}$ for different Φ_0. (b) Variation of Φ_1 with $c^0_{\mathrm{Li}^+}$ for different Φ_0. (c) Variation of j with potential difference $\Phi_0 - \Phi_1$ in 1D NEDL. (d) Variation of Φ_1 with Φ_0. (e) Variation of j with L for different Φ_0. (f) Variation of Φ_1 with L for different Φ_0.

Figure 3(c) illustrates an exponential correlation between j and the potential difference $\Phi_0 - \Phi_1$ in the 1D NEDLs. However, there is a deviation from the strict exponential behavior predicted by the Butler–Volmer equation. The NEDL significantly raise the Li^+ concentration at the reaction interface while requiring minimal potential drop. Consequently, the current predicted by the 2D NEDL model is lower than that predicted by Butler–Volmer.

Figure 3(d) shows a near-linear correlation between Φ_0 and Φ_1 at lower Φ_0 and an exponential correlation at high Φ_0. The exponential dependence of j on $\Phi_0 - \Phi_1$ [Fig. 3(c)] dominates at high potentials region. At lower potentials, the increasing electromigration is required to match the increasing j. That results in potential drop across Φ_1 which causes the transition to linear coupling behavior.

The charge density σ integrates the collective effects of Φ_0, electrode morphology, and 2D electrostatic boundary conditions on j. Given this complex interplay, we focus on the role of σ in lithium dendritic growth instead of its mechanics. Through Eq. (5), σ is converted to L, which translates the boundary conditions of the 2D NEDL to the 1D NEDLs. Subsequent discussions will focus on analyzing the characteristics of L instead of σ.

Figure 3(e) shows that j is inversely proportional to L as defined by Eq. (S9) of the SM and the deviation from strict inverse behavior originates from the dependence of Φ_1 on L [Fig. 3(f)]. Crucially, this functional form exhibits a characteristic steepening region where reduction current surges. As Φ_0 moves in the more negative direction, the steep transition zone shift toward larger L, thereby reducing the critical net charge density σ required to initiate dendritic growth. Concurrently, a more negative Φ_0 leads to a higher σ across the 2D NEDL [Fig. 3(d)]. This dual effects of the reducing nucleation threshold and increasing charge driving force synergistically promotes dendritic growth at lower curvature variations. This result explains the experimental transition from needle-like to mossy morphology under strong polarization.[34] However, σ does not necessarily peak at the tip for complex electrode morphology (e.g., bowl-shaped electrodes). As a result, j at the tips may not be the highest either.[35,36]

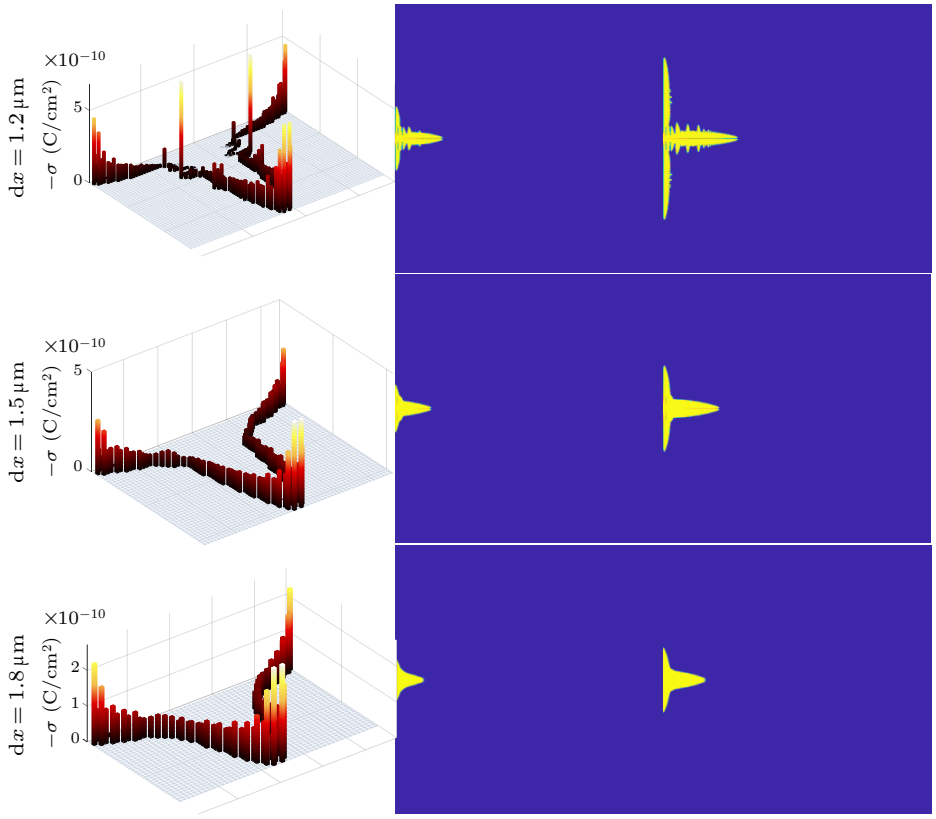

Fig. 4. Surface charge density σ at $t = 5\,\mathrm{s}$ (left), order parameter evolution at $t = 5\,\mathrm{s}$ and $t = 15\,\mathrm{s}$ (middle/right) across spatial steps $\mathrm{d}x = 1.2\,\mu\mathrm{m}$, $1.5\,\mu\mathrm{m}$, and $1.8\,\mu\mathrm{m}$. Simulated at $\Phi_0 = -4.04\,\mathrm{V}$, initial bulk ions concentration of $1\,\mathrm{mol/L}$ and the environment of 2D NEDL.

Quantitative analysis of charge density effects on lithium dendrite growth remains challenging for both conventional 1D NEDL and phase field models. Thus, we carry out phase field simulations on a 300×300 grid with different spatial steps to investigate these effects on the 2D NEDL. By maintaining morphologically identical semi-elliptical nuclei [we set $(\frac{x}{6.6674})^2 + (\frac{y-150}{3.3337})^2 \leqslant 1$] while systematically reducing the grid discretization spatial steps ($1.8\,\mu\mathrm{m}$, $1.5\,\mu\mathrm{m}$, and $1.2\,\mu\mathrm{m}$), we achieve progressive reduction in the simulated nucleus size and consequently increase in surface curvature ($\kappa_0 \propto 1/\mathrm{d}x$). This controlled increase of σ at $\Phi_0 = -4.04\,\mathrm{V}$ enables direct interrogation of its influence on dendritic propagation.

Figure 4 illustrates that finer spatial discretization results in greater nucleus curvature and more pronounced dendritic propagation (we display the potential distribution in SM Fig. S5). At the grid step of $1.2\,\mu\mathrm{m}$, pronounced side-branch formation emerges attributable to curvature-induced reduction of L along the dendrite flanks. When $L(r)$ enters the steep region of the $j(L)$ curve [Fig. 3(e)], the local sensitivity $\frac{\partial j}{\partial L}$ undergoes a surge, reaching values orders of magnitude higher than in the pre-transition region. This abrupt sensitivity magnifies minor variation in L into substantial current heterogeneity, initiating side-branch nucleation. The incipient protrusions then further amplify the heterogeneity of L through curvature autocatalysis, yielding well-developed side-branch architectures by $t = 25\,\mathrm{s}$.

However, dendrite proliferation inherently expands the electrode surface area, leading to reduction of σ and increase of L. Consequently, nascent side branches unexposed to the steepening region's high-sensitivity regime during early growth exhibit diminishing probability of later development. Thus, each Φ_0 defines a critical nucleus size determined by the L-position where current surge initiates in Fig. 3(e) (it can be calculated by simulating in different $\mathrm{d}x$). Nuclei smaller than this threshold is prone to runaway side-branching formation.

The growth rate of dendrite tip accelerates with the increasing of the nucleus curvature, as shown in Fig. 4. At $t = 5\,\mathrm{s}$, for the grid spatial steps of $1.2\,\mu\mathrm{m}$, $1.5\,\mu\mathrm{m}$, and $1.8\,\mu\mathrm{m}$, the L at the dendrite tip are $12\,\mu\mathrm{m}$, $16\,\mu\mathrm{m}$, and $26\,\mu\mathrm{m}$, respectively. The corresponding current density j values are $21\,\mathrm{A/cm^2}$, $16\,\mathrm{A/cm^2}$, and $10\,\mathrm{A/cm^2}$, and the corresponding surface charge density σ values are $-6.1 \times 10^{-10}\,\mathrm{C/cm^2}$, $-4.4 \times 10^{-10}\,\mathrm{C/cm^2}$, and $-2.7 \times 10^{-10}\,\mathrm{C/cm^2}$, respectively. The uniform charge density from the tip effect controls dendrite growth via Eq. (5) and $\mathcal{F}' : (\Phi_0, \gamma_t, c^0_{\mathrm{Li}^+}, L) \mapsto v$ [see Fig. 3(e)]. Therefore, dendrite height and the tip effect can be suppressed by increasing nucleus size to reduce curvature—particularly in cases where uniform nucleation is unattainable.

In summary, this study proposes a strategy of reducing the dimensionality of 2D electric field data to train FCNN [$\mathcal{F} : (\Phi_0, \gamma_t, L, c^0_{\mathrm{Li}^+}) \mapsto \Phi_1$], enabling the decomposition of 2D NEDL under arbitrary boundary conditions. The

influence of σ and the tip effect in dendrite growth in 2D NEDL are further quantitatively analyzed. The approach allows to extend modelling of finer-scale electrochemical phenomena including ion-specific Stern layer, desolvation kinetics and auxiliary ions intercalation to the macroscale level. More broadly, the dimensionality-decomposition strategy will be the key to modeling 2D solid–solid interface behaviors such as local non-uniform contact and crack formation.[37]

Acknowledgements. This work was supported by the National Natural Science Foundation of China (Grant Nos. 92472207, 52472223, and 92572301). The authors appreciate the High-Performance Computing Center of Shanghai University for providing the computing resources and technical support.

References

[1] Genet S, Costalat R, and Burger J 2000 *Acta Biotheor.* **48** 273
[2] Galla H J and Sackmann E 1975 *Biochim. Biophys. Acta* **401** 509
[3] Yuan H, Shimotani H, Tsukazaki A, Ohtomo A, Kawasaki M, and Iwasa Y 2009 *Adv. Funct. Mater.* **19** 1046
[4] Bisri S Z, Shimizu S, Nakano M, and Iwasa Y 2017 *Adv. Mater.* **29** 1607054
[5] Chen C, Jin H, Wang P, Sun X, Jaroniec M, Zheng Y, and Qiao S Z 2024 *Chem. Soc. Rev.* **53** 2022
[6] Tessier F and Slater G W 2006 *Electrophoresis* **27** 686
[7] Li C K, Zhang J, and Huang J 2022 *J. Chem. Phys.* **157** 184704
[8] Duplantier, Goldstein, Romero-Rochn V, and Pesci A I 1990 *Phys. Rev. Lett.* **65** 508
[9] Wu J 2022 *Chem. Rev.* **122** 10821
[10] He R, Chen S L, Yang F, and Wu B L 2006 *J. Phys. Chem. B* **110** 3262
[11] Zhang L, Cai J, Chen Y, and Huang J 2021 *J. Phys.: Condens. Matter* **33** 504002
[12] Jarvey N, Henrique F, and Gupta A 2022 *J. Electrochem. Soc.* **169** 093506
[13] Levey K J, Edwards M A, White H S, and Macpherson J V 2023 *Phys. Chem. Chem. Phys.* **25** 7832
[14] Van Soestbergen M 2012 *Russ. J. Electrochem.* **48** 570
[15] Marcicki J, Conlisk A T, and Rizzoni G 2014 *J. Power Sources* **251** 157
[16] Zhang C, Lu S, Mao R, Chen W, Tan L, Zhou Q, and Yang J 2017 *J. Appl. Phys.* **121** 044502
[17] Wang H and Pilon L 2013 *J. Power Sources* **221** 252
[18] Helmholtz H V 1853 *Ann. Phys.* **165** 353
[19] Stern O 1924 *Z. Elektrochem. Angew. Phys. Chem.* **30** 508
[20] Newman J and Balsara N P 2004 *Electrochemical systems* 4nd edn. (Hoboken, NJ: John Wiley & Sons Inc.) p. 517
[21] Brissot C, Rosso M, Chazalviel J N, Baudry P, and Lascaud S 1998 *Electrochim. Acta* **43** 1569
[22] Tan J, Cannon A, and Ryan E 2020 *J. Power Sources* **463** 228187
[23] Bieker G, Winter M, and Bieker P 2015 *Phys. Chem. Chem. Phys.* **17** 8670
[24] Liu Y, Zou X, Yang Z, and Shi S 2022 *J. Chin. Ceram. Soc.* **50** 863 (in Chinese)
[25] Zhang J, Liu Y, Wang C, and Tan H 2021 *J. Electrochem. Soc.* **168** 090522
[26] Gao L and Guo Z 2020 *Comput. Mater. Sci.* **183** 109919
[27] Zhang R, Shen X, Zhang Y T, Zhong X L, Ju H T, Huang T X, Chen X, Zhang J D, and Huang J Q 2022 *J. Energy Chem.* **71** 29
[28] Pant B R, Ren Y, and Cao Y 2024 *ACS Appl. Mater. Interfaces* **16** 56947
[29] Han D and Lin C 2025 *Energy Storage Mater.* **74** 103982
[30] Chen L, Zhang H W, Liang L Y, Liu Z, Qi Y, Lu P, Chen J, and Chen L Q 2015 *J. Power Sources* **300** 376
[31] Valøen L O and Reimers J N 2005 *J. Electrochem. Soc.* **152** A882
[32] Sun C, Gao L, Rong W, Yang Y, and Bai Y 2025 *Chem. Eng. J.* **503** 158148
[33] Rey I, Bruneel J L, Grondin J, Servant L, and Lassègues J C 1998 *J. Electrochem. Soc.* **145** 3034
[34] Kong L, Xing Y, and Pecht M G 2018 *IEEE Access* **6** 8387
[35] Harry K J, Higa K, Srinivasan V, and Balsara N P 2016 *J. Electrochem. Soc.* **163** A2216
[36] Ye W, Wang L, Yin Y, Fan X, Cheng Y, Gao H, Zhang H, Zhang Q, Luo G, and Wang M S 2021 *ACS Energy Lett.* **6** 2145
[37] Swift M W, Swift J W, and Qi Y 2021 *Nat. Comput. Sci.* **1** 212